Research Article

Ion Imaging of Native Protein Complexes Using Orthogonal Time-of-Flight Mass Spectrometry and a Timepix Detector

Anjusha Mathew, Ronald Buijs, Gert B. Eijkel, Frans Giskes, Andrey Dyachenko, Jerre van der Horst, Dimitry Byelov, Dirk-Jan Spaanderman, Albert J. R. Heck, Tiffany Porta Siegel, Shane R. Ellis,* and Ron M. A. Heeren*

Read Online

ACCESS | Metrics & More | Article Recommendations | SI Supporting Information

ABSTRACT: Native mass spectrometry (native MS) has emerged as a powerful technique to study the structure and stoichiometry of large protein complexes. Traditionally, native MS has been performed on modified time-of-flight (TOF) systems combined with detectors that do not provide information on the arrival coordinates of each ion at the detector. In this study, we describe the implementation of a Timepix (TPX) pixelated detector on a modified orthogonal TOF (O-TOF) mass spectrometer for the analysis and imaging of native protein complexes. In this unique experimental setup, we have used the impact positions of the ions at the detector to visualize the effects of various ion optical parameters on the flight path of ions. We also
demonstrate the ability to unambiguously detect and image individual ion events, providing the first report of single-ion imaging of protein complexes in native MS. Furthermore, the simultaneous space- and time-sensitive nature of the TPX detector was critical in the identification of the origin of an unexpected TOF signal. A signal that could easily be mistaken as a fragment of the protein complex was explicitly identified as a secondary electron signal arising from ion-surface collisions inside the TOF housing. This work significantly extends the mass range previously detected with the TPX and exemplifies the value of simultaneous space- and time-resolved detection in the study of ion optical processes and ion trajectories in TOF mass spectrometers.

KEYWORDS: *Native mass spectrometry, Orthogonal time-of-flight mass spectrometry, Timepix detector, Ion optics, Single-ion imaging*
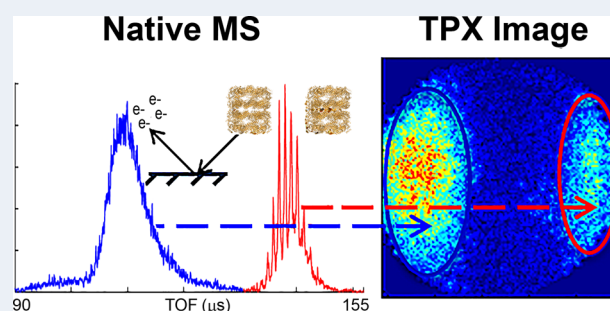
INTRODUCTION

Advances in electrospray ionization (ESI) over the past two decades have enabled the ionization and mass analysis of macromolecular assemblies (MMAs) in their pseudonative state, where noncovalent interactions are maintained, a method referred to as native mass spectrometry (native MS).[1] Using native MS, various structural details of MMAs such as topology, stoichiometry, subunit connectivity, dynamics, and interaction of large biomolecules like protein complexes,[2,3] protein–ligand complexes,[4,5] protein–nucleic acid complexes,[6,7] and virus capsids[8,9] have been successfully investigated.

A combination of a nano-ESI source[10,11] and an orthogonal time-of-flight (O-TOF) mass analyzer equipped with an ion reflectron[12,13] is widely used for native MS. Careful consideration in the design and operating parameters of the ion transfer optics is critical for the transmission of the high mass-to-charge (*m/z*) ions produced under native conditions. Elevated gas pressures and radio frequency ion guides operating with higher amplitudes and/or lower frequencies are often used to enhance the transmission of high *m/z* ions into the TOF (or other) mass analyzer.[14–17] Ion detection in TOF-MS is generally accomplished using microchannel plates

(MCPs)[18] in combination with time-to-digital converters (TDCs) or analog-to-digital converters (ADCs) that are typically capable of single-ion detection.[19,20] While these are popular and versatile detection systems deployed in virtually all modern TOF instruments, they do not provide spatial information on ions arriving at the detector surface. This poses a limitation as these impact coordinates can encode critical information on the trajectories that ions take through the intermediate ion optics and TOF analyzer. As a result, they may reveal ion optical processes that remain hidden if only the resulting integrated mass spectrum is observed. In this study, we have coupled an active pixelated detector (Timepix (TPX)) for the first time to an O-TOF mass spectrometer modified for native MS to study the ion transport processes of large proteins and protein complexes.
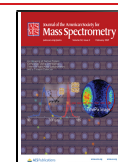
The TPX is a position- and time-sensitive charge detector consisting of a 512×512 pixel array of 55 μm pitch, with each pixel capable of recording both the arrival time and impact coordinates of impinging particles.[21] Initially developed for high energy physics applications where a silicon sensor layer is placed on top of the detector chip for localized charge generation from impacting particles,[22−25] it has also been adapted for ion imaging in MS applications.[26−35] In MS applications, a TPX detector chip without a silicon sensor layer is positioned behind a dual MCP and directly detects the amplified electron pulses emitted by the MCP. Initial TPX studies focused on the development of stigmatic ion imaging applications using both secondary ion mass spectrometry (SIMS) and matrix-assisted laser desorption/ionization (MALDI) with the goal to improve the spatial resolution and throughput of mass spectrometry imaging experiments.[27,31,33] Improvements in detection efficiencies for higher mass ions such as intact proteins was subsequently realized by the development of a TPX detection system biased at a high voltage (HV) of +12 kV/−8 kV for ion post-acceleration prior to ion detection.[30] Furthermore, the coupling of the TPX detector to a commercial MALDI-axial-TOF instrument (Ultraflex III from Bruker Daltonics) demonstrated both the ability to detect ions with m/z values up to 400,000[29] and the study of m/z-dependent ion trajectories defined by mass-independent initial ion velocities and the ion extraction optics.[32] These studies clearly show the significance of spatially and temporally resolved ion detection for studying ion optical processes in mass spectrometry.

In this work, we describe the development of a new HV-floating TPX detection system and its coupling to an O-TOF LCT mass spectrometer modified for high mass transmission and equipped with a nano-ESI ion source, thereby providing the first report for the detection and imaging of highly charged ions with molecular weights in excess of 800 kDa using TPX technology. In this system, we have used the spatial and temporal distributions of ions arriving at the detector as a readout to investigate ion transport properties through the different ion optics elements of the instrument and to resolve individual ion detection events in both space and time. Furthermore, we discuss how both the impact coordinates and arrival time information recorded by the TPX detector are utilized to explain an unusual signal in the native mass spectrum, which was also observed in earlier studies using modified quadrupole-TOF (q-TOF) I, q-TOF II, and LCT mass spectrometers (Micromass, Manchester, UK) under certain ion optical conditions but could not be explained solely by the TOF spectrum generated by conventional mass spectrometers.[36−41]

MATERIALS AND METHODS

Materials. Cytochrome c (12.4 kDa) from equine heart, myoglobin (17.6 kDa) from equine heart, pepsin (35 kDa) from porcine gastric mucosa, bovine serum albumin (BSA, 66.4 kDa), conalbumin (77 kDa) from chicken egg white, concanavalin A (102 kDa) from *Canavalia ensiformis*, immunoglobulin G (IgG, ~150 kDa) from human serum, beta amylase (β-amylase, 223.8 kDa) from sweet potato, chaperonin 60 (GroEL, ~800 kDa) from *Escherichia coli*, ammonium acetate, tris-acetate, potassium chloride, ethyl-enediaminetetraacetic acid (EDTA), adenosine-5′-triphosphate (ATP), magnesium chloride, ammonium hydroxide, and acetic acid were all purchased from Sigma-Aldrich

(Zwijndrecht, The Netherlands). Methanol, acetone, and LC-MS grade water were purchased from Biosolve (Valkenswaard, The Netherlands).

Nanospray needles were homemade from preheated borosilicate glass capillaries (Science Products GmbH, Hofheim, Germany) on a DMZ universal electrode puller (Zeitz-Instruments Vertriebs GmbH, Munich, Germany) followed by gold coating with a SC7640 sputter coater (Quorum Technologies, Kent, UK).

Sample Preparation. The lyophilized protein assemblies (except GroEL) were dissolved to a stock concentration of 100 μM in LC-MS grade water. These samples were further diluted to a final monomer concentration of 2.5−20 μM in 100 mM ammonium acetate (pH 6.8) prior to MS experiments. The preparation of GroEL samples was performed as follows. A 5.8 μM (monomer concentration) solution of GroEL was made in buffer A (20 mM tris-acetate, 50 mM potassium chloride, 0.5 mM EDTA, 1 mM ATP, 5 mM magnesium chloride adjusted to pH 8). This solution vortexed slowly for 1 h followed by the addition of ice-cold methanol (20% of final volume). The solution was equilibrated by vortexing another 1 h followed by the addition of ice-cold acetone (50% of final volume) and kept overnight at −20 °C to precipitate the protein. Precipitated GroEL was redissolved in 500 μL of buffer A, which was subsequently shaken for 20 min at room temperature. This sample was buffer exchanged with 100 mM ammonium acetate at pH 6.8 using 30 kDa molecular weight cutoff (MWCO) Amicon Ultra centrifugal filter (Millipore, Merck KGaA, Germany) to a final monomer concentration of 28 μM.

Timepix Detector. The TPX detector family was developed within the Medipix consortium hosted by the European Organization for Nuclear Research (CERN, Geneva, Switzerland).[21] A single TPX chip consists of a 256×256 pixel array having a pixel pitch of 55 μm and dimensions of 1.4×1.6 cm^2. For this study, we used a 2×2 quad array consisting of 512×512 pixels in total. Each pixel is a single stop TDC that registers an event once the input charge of a given pixel exceeds a certain threshold (equivalent to ~600 electrons). The TPX is positioned 2 mm behind a dual microchannel plate and thus detects the emitted electron pulses that span multiple pixels.[27] Each TPX pixel can be operated in three modes: (i) counting mode, in which each pixel counts the number of arriving particles; (ii) time-of-arrival (TOA) mode, in which the arrival time of each particle is measured with respect to an external trigger; and (iii) time-over-threshold (TOT) mode, in which each pixel registers the time for which the signal is above a certain detection threshold level. In this study, TOA mode is used and the TPX data are read out via a ReLAXD (high-Resolution Large-Area X-ray Detector) readout board with a speed of 1 Gbit·s$^{−1}$.[42]

Mass Spectrometer and Detection System. All experiments were performed on two similar LCT O-TOF mass spectrometers (Micromass, Manchester, UK); one is a modified LCT with the described TPX detector (Maastricht University, Maastricht, The Netherlands), and the other is a standard LCT (Utrecht University, Utrecht, The Netherlands). Both instruments were modified to improve the transmission of high m/z ions, through the installation of a speedivalve that reduces the pumping efficiency of the rotary pump and thus increases the pressure in the source region. The systems were additionally equipped with a flow restriction sleeve in front of the first hexapole to increase the pressure in the RF optics.
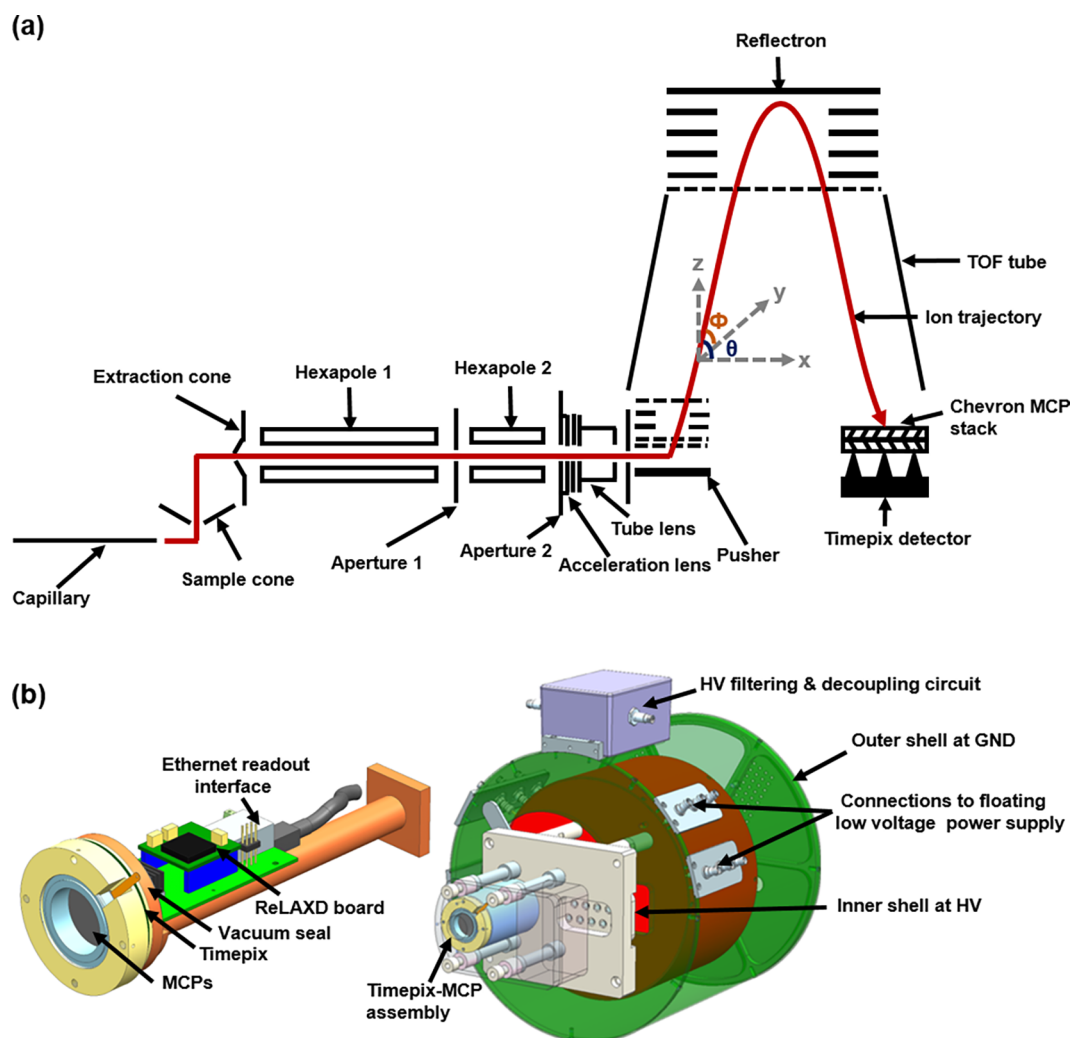
Figure 1. (a) Schematic of the ion optics of modified LCT O-TOF mass spectrometer. The TPX detector is positioned behind the MCP stack. Ions (red trace) are initially accelerated and transported in the x-direction and subsequently accelerated in the z-direction before they enter the O-TOF analyzer. The detector assembly is positioned in the $x-y$ plane. Flight angles Φ and θ defines the ion trajectory. (b) Schematic representation of mechanical design of MCP-TPX setup. The MCP-TPX assembly is isolated from the readout electronics via a vacuum seal (left) and placed within the inner shell kept at HV and protected by the outer shell at ground potential (right).

Such elevated pressures in these regions are critical for the gentle transmission of high m/z ions through collisional damping.[14−16,43,44]

A schematic of the ion optics of the instrument is shown in Figure 1a. Ions generated using an in-house built static nano-ESI source are transferred into an orthogonal acceleration TOF mass analyzer via two differentially pumped hexapole RF lenses. The interface between the nano-ESI source and MS consists of two cones: a sample cone and an extraction cone (source region). Apertures 1 and 2 are used to focus ions into the hexapole region and a set of lenses (acceleration, focus, steering, and tube lenses) are used to transfer the beam into the pusher region for TOF based mass analysis.

The LCT is designed such that the field-free TOF tube is floating at HV (typically −4.6 kV in positive ion mode), and as such, the TPX detector and associated readout electronics must also operate at HV to enable operation of the instrument using the standard acceleration schemes. A schematic of the detector assembly is shown in Figure 1b and is based on a previously reported HV-TPX design.[30] The inner shell is floated at HV and contains the TPX detector in vacuum and

the associated ReLAXD readout system at atmospheric pressure. A multifunctional chip carrier provides both vacuum seal and electrical feedthroughs for connection from the TPX to the ReLAXD board. The inner shell is surrounded by an outer shell shield that is kept at ground potential. A home-built floating low voltage power supply was used to power up the TPX, ReLAXD readout board, and cooling system. An external power supply (FuG Elektronik GmbH, Schechen, Germany) provides a voltage offset to the TPX relative to the back MCP to attract the amplified electrons toward the TPX surface (typically +800 V offset). The bias between the front and back MCP plates was 1.6 kV and controlled by the standard MassLynx software. An optical fiber protocol via two ethernet media converters (N-Tron 1002MC) was used to transfer the TCP/IP signal output at HV from the ReLAXD board to the acquisition PC at ground potential. The TPX was triggered using a down-sampled version of the main trigger pulse that starts the orthogonal acceleration in the pusher. The trigger was down-sampled to a rate of 30−50 Hz to match the achievable frame rate of the TPX. This down-sampled trigger passed through a digital pulse and delay generator (DG535,

Stanford Research Systems) to trigger and open the TPX for the measurement period and have flexible timing control. Trigger was converted to optical domain for the HV isolation, and two home-built converters were used for the signal transmission from the pulse and delay generator to the TPX. All experiments were performed using a 20 ns TPX clock width, corresponding to a maximum measurement window of 236.2 μs for each TOF cycle. Typical flight times were <155 μs for all data reported here.

Samples were introduced into the mass spectrometer using gold-coated needles via an in-house built static nano-ESI source. Three microliters of each sample was loaded into the needle, and a spray voltage of 1.4 kV was applied. Sample cone voltage, extraction cone voltage, RF lens voltage of hexapoles, and the pressures in source and TOF analyzer regions were optimized for each protein separately. All spectra were recorded using the following voltage settings; DC offset 1 = 10 V, DC offset 2 = 6 V, ion energy = 10 V, aperture = 20 V, TOF tube = 4600 V, reflectron = 1000 V, MCP gain = 1600 V, and TPX = −2200 V unless stated otherwise. All ion optics parameters except the TPX voltage were defined via MassLynx V4.1 software (Waters, Wilmslow, UK).

Data Acquisition and Analysis. The SoPhy (Software for Physics) software package was used for the TPX chip control and data acquisition (Amsterdam Scientific Instruments, Amsterdam, The Netherlands). Ten thousand TOF cycles were collected and summed for each data set. For each TOF cycle, a separate data file was saved that registers the information about the pixel addresses (location) and corresponding TOA associated with each event. These raw files were subsequently analyzed using in-house developed software written in MATLAB (R2014a, MathWorks Inc., Natick, MA, USA).

Ion Optics Simulations. SIMION 8.1 (Scientific Instrument Services, Ringoes, USA) software was used for all ion optics simulations to evaluate the experimental results. A two-dimensional model of the simplified TOF geometry of the LCT generously provided by Waters Corporation (Wilmslow, UK) was used for the simulations.

■ RESULTS AND DISCUSSION

Detection of High Mass Native Proteins Using Timepix. We acquired mass spectra of native GroEL (800 kDa) under the same ion optical conditions on both the TPX-equipped LCT and one equipped with the standard MCP/TDC detection system to first validate the native MS data recorded by the TPX system. The resulting native mass spectra collected on both the instruments are shown in Figure 2. Each spectrum represents a 1 s accumulation time corresponding to 45 and 7143 pusher pulses for MCP-TPX and MCP-TDC data, respectively. In both MCP-TPX and MCP-TDC generated spectra, a series of peaks spanning over the m/z values between 11,290 and 12,740 are observed. This is consistent with the previously reported native GroEL spectrum[45] and corresponds to the 63+ to 71+ charge states. We note the lower mass resolution of the MCP-TPX spectra. In part, this can be explained by known time-walk effects, whereby a single electron pulse is registered across several time bins (Supporting Information Figure S1).[27,46−48] Previous studies demonstrated that centroiding approaches can be used to correct for time-walk effects and improve the effective mass resolution.[27,46,49] Here, we found such approaches to provide a minimal improvement in mass resolution for the detection of
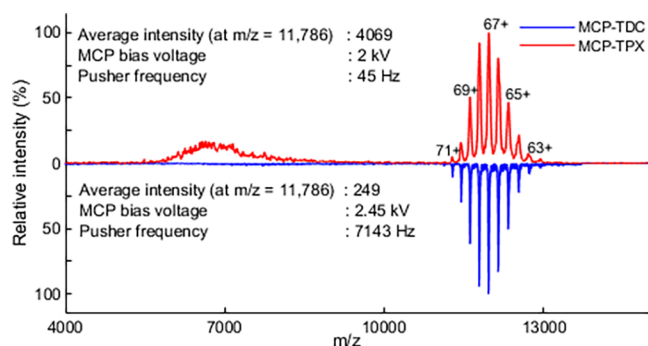

Figure 2. Averaged mass spectra of native GroEL acquired on an LCT equipped with TPX detector (top, red trace) and on a standard LCT with conventional MCP-TDC detector (bottom, blue trace). Both spectra were acquired under identical ion optical conditions (DC offset 1 = 10 V, DC offset 2 = 6 V, ion energy = 30 V, aperture = 20 V, TOF tube = 4600 V, reflectron = 1000 V). The MCP-TPX is the result of the accumulation of 45 pusher pulses, whereas the MCP-TDC is the result of 7143 pusher pulses.

the high m/z ions. This suggests the lower mass resolution of the TPX compared to the conventional detection system is caused by some other phenomena. Nonetheless, this mass resolution is still sufficient to resolve the multiply charged high m/z native species generated by ESI.

The differences in absolute intensity values arise from the different nature of each detection approach. In the case of the standard LCT system, the MCP-TDC records the number of time bins for which an ion event is registered during each measurement cycle with a digitization rate of 1 GHz. This detector output is then converted to counts per second. In the case of the TPX, the output value corresponds to the average number of pixels activated for each arrival time, with individual events typically spread across the majority of the detector surface. Each event results in an electron pulse that spans 6−65 pixels, thus multiple counts are recorded for each ion event. It is noteworthy that the TPX data were acquired with 158 times fewer pusher pulses than that used to acquire the TDC spectrum.

The TPX may provide improved sensitivity for high mass ions due to the lower charge threshold for event registration.[29] Given the high m/z range observed, some ion impacts can result in lower ion-to-electron conversion efficiency and thus lower overall amplification. Some of these events may still be registered by the TPX but do not exceed the detection threshold of the standard TDC (∼70 mV). However, such comparisons are difficult to quantify. A second potential advantage of the TPX is the ability to differentially detect simultaneous individual ion events that arrive at different positions, whereas this is not possible with the conventional integrating TDC system. While this can potentially lead to a benefit for the TPX at high count rates, in such O-TOF instruments, the number of ions per pusher pulse is sufficiently low that it is likely not to have a significant effect.

The TPX data also exhibit a broad lower TOF distribution corresponding to arrival times of 90−130 μs (appearing at m/z hump ranging from 5500 to 9000). The potential origin of this distribution is discussed later in this article.

Single-Ion Imaging of Protein Complexes. Single-ion detection of MMAs has been previously reported on TOF,[8,50] Fourier transform ion cyclotron resonance (FT-ICR),[51,52] and Orbitrap[17,53] platforms. Recent works on individual ion
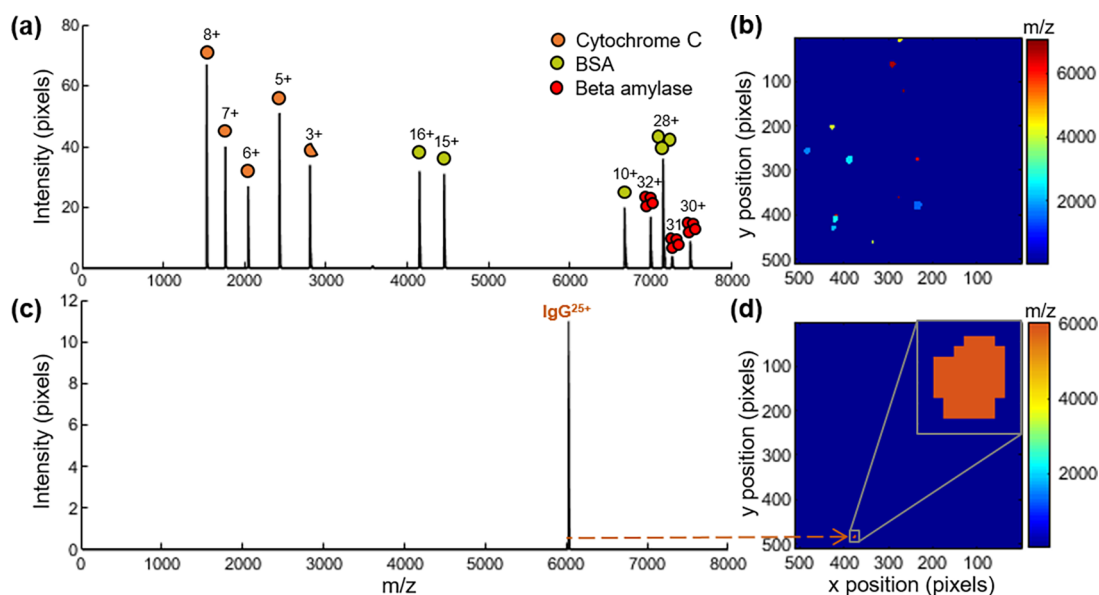
Figure 3. (a) Mass spectrum and (b) TPX image acquired from a single TOF cycle (one TPX frame) using a protein mix of cytochrome c, BSA, and β-amylase sprayed under native conditions. (c) Mass spectrum and (d) TPX image acquired from a second single TOF cycle using IgG. Only a single-ion event that represents IgG^{25+} is detected. The y-axis in (a) and (c) represents the number of TPX pixels activated for each ion event. Each color in the single frame TPX image corresponds to a different m/z or arrival time.

measurement using Orbitrap analyzers demonstrated the ability to significantly improve mass resolution at high m/z values[54] and allowed precise mass determination and charge detection of highly complex mixtures of MMAs.[55,56] In this section, we demonstrate for the first time the capabilities of an LCT-TPX assembly for simultaneous space- and time-resolved detection of single MMA ions.

Figure 3a,b shows the mass spectrum and measurement frame image generated from a single TOF cycle using a protein mix containing cytochrome c (12.4 kDa), BSA (66.4 kDa), and β-amylase (223.8 kDa), three commonly used molecular weight markers in gel filtration chromatography. Each impact event in the single frame image (Figure 3b) corresponds to the electron footprint of single-ion event at the MCP and is associated with a single peak in the mass spectrum (Figure 3a), thereby demonstrating single-ion detection and imaging of protein complexes. Figure S2 (Supporting Information) contains single frame spectra and images from four different TOF cycles. Each peak in the single frame spectrum may correspond to more than one ion event if more ions arrive at the same time but strike at different locations of the detector. The number of pixels activated by each ion event is related to the number of electrons emitted from the MCP, which in turn is related to the efficiency of the initial ion-to-electron conversion, amplification steps though the channels of MCP, and the space charge-driven expansion of the electron pulse between the MCP and TPX. These processes are expected to follow Poisson statistics and produce a distinctive distribution of the size of each electron showers footprint on the TPX detector.[57]

Figure 3c,d shows data from another single TOF cycle in which only one ion event is recorded. This ion event is assigned to IgG^{25+} at m/z = 6029. In this case, the electron footprint of IgG^{25+} occupies 46 pixels and results in a maximum time-bin intensity of 11 counts with a TOF spread of 180 ns (Supporting Information Figure S1). Given the fact that the pulse width of a single MCP pulse is expected to be no

longer than several nanoseconds, this widespread of TOF values for a single-ion event is due in part to the time-walking effects of TPX.[27,46−48]

Influence of Ion Optics on the Spatial Distribution of the Ions Arriving at the Detector. We next investigated the ability of the TPX to study ion trajectories as a function of various ion optical parameters. In the LCT schematic diagram shown in Figure 1a, ions are initially accelerated in the x-direction as they leave the ion source and travel toward the pusher. The pusher pulses the ions in the z-direction for the TOF and the spatial profile measurements and finally detected by the MCP-TPX assembly in the $x−y$ plane. The impact coordinates of ions at the detector are determined by the flight angles of the ion beam leaving the pusher. The flights angles θ and Φ indicated in Figure 1a and given by

$$\vartheta = \tan^{-1}\frac{v_z}{v_x} \quad \Phi = \tan^{-1}\frac{v_z}{v_y} \tag{1}$$

where v_x, v_y, and v_z are the velocity components in x-, y-, and z-directions, respectively. In the region prior to the pusher, the velocity components in y- and z-directions are significantly smaller than the axial (x) velocity component of the ion beam. Once the beam is accelerated to the z-direction by the orthogonal pusher, v_z increases significantly, whereas v_x and v_y remain almost unchanged. Hence, the ion trajectory in the post-pusher region is mainly determined by the flight angles defined by equation set 1. As no voltage source accelerates the ions in the y-direction, v_y is much smaller than v_z, which keeps $\Phi \approx 90°$. As a result, no shift in impact position is observed along the y-direction when any of the instrument settings are altered, even for the parameters that affect the v_z component. That means θ is the only significant flight angle that defines the impact position of the ion cloud. As a result, only shifts in the spatial profile along the x-direction under normal operating conditions are expected.

We have observed that only four ion optical parameters have a critical influence of the spatial distribution of ions in the
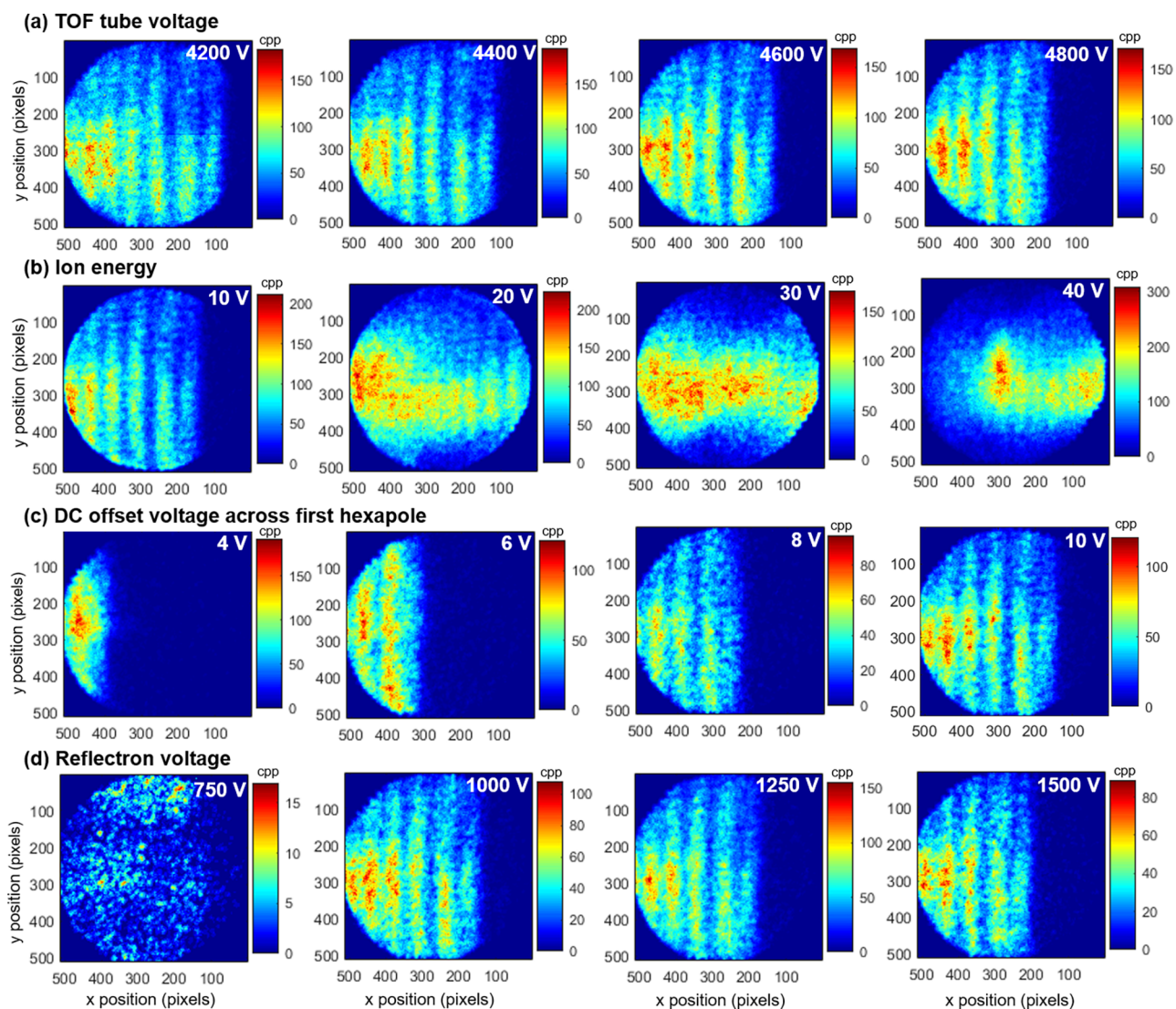
Figure 4. Influence of (a) TOF tube voltage, (b) axial ion energy, (c) DC offset voltage across first hexapole, and (d) reflectron voltage on the spatial distribution of cytochrome *c* ions arriving at the detector. All data represents the sum of 5000 TOF cycles by spraying native cytochrome *c* under identical voltage conditions and represent the sum of all charge states (cpp = counts per pixel).

detection plane: TOF tube voltage, axial ion energy, DC offset across the first hexapole, and reflectron voltage. No significant shift in the ion profile along *x*-direction was observed for change in any of the other ion optics settings other than these parameters as all other voltage elements only alter the potential energy profile locally. This will be discussed in more detail below.

Effect of TOF Tube Voltage. The spatial distribution of the cytochrome *c* ion cloud recorded at different TOF tube voltages is shown in Figure 4a. The entire *m/z* range that encompasses all detected charge states was summed for this evaluation. The vertical patterns in the *y*-direction that appear as "ion shadows" in the image are explained by the transmission grids placed in the acceleration region.

The "TOF tube" defines the voltage at the exit of the pusher and thus determines the orthogonal acceleration energy of the ions as they enter the field-free TOF tube. The cytochrome *c* mass spectrum appears almost similar for different TOF tube voltages (Supporting Information Figure S3), but the spatial distribution of the ion cloud at the detector shifts toward left as the TOF voltage increased from 4200 to 4800 V. These results

can be explained as follows: a higher TOF tube voltage increases the total acceleration potential of the pusher and thus increases v_z, whereas v_x and v_y remain unchanged, and thus raises the flight angle θ. At a TOF tube voltage of 4200 V, the reduced θ angle combined with the width of the ion beam in the *x*-direction results in most of the ion beam hitting detector. A higher TOF tube voltage increases the flight angle and thus leads to a larger fraction of the ion beam missing the detector.

Effect of Axial Ion Energy. The impact of "ion energy" on the spatial distribution of the ion cloud is shown in Figure 4b. The "ion energy" settings defines the voltage at aperture 1, and all voltage elements prior to the pusher entrance (except capillary) are defined with respect to the aperture 1; thus this parameter ultimately determines the axial ion energy of ions entering the pusher. Higher ion energies increase the axial velocity and thus reduces θ, so that the ion cloud moves toward the right of the detector.

The intensity distribution of the ion cloud appears different at lower ion energies. This can be explained by the increased sensitivity of the ion optics to voltage changes at lower ion
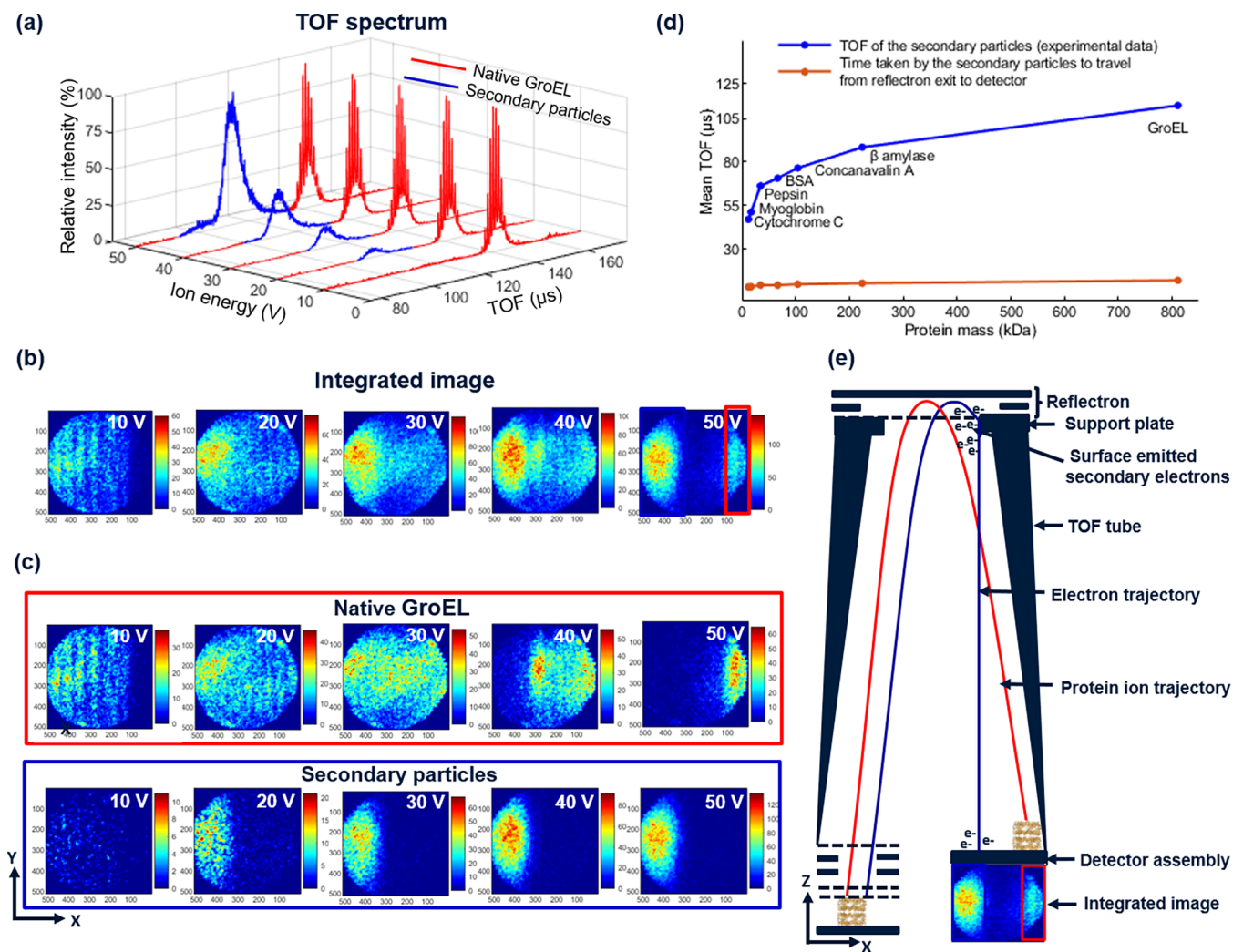
Figure 5. (a) TOF spectra and (b) spatial distribution at the TPX detector for native GroEL recorded at different axial ion energies (10−50 V). (c) TPX images generated separately for native GroEL (red trace in panel a) and secondary particles (blue trace in panel a) at different ion energies. (d) Comparison between the mean TOF of the secondary particles (blue) and time difference between simulated mean TOF of GroEL to reach the support plate at the exit of the reflectron and measured TOF of secondary particles at the detector. (e) Schematic diagram explains the generation of secondary particles from the parent GroEL ion. At higher ion energies, a fraction of the wide ion beam hits the support plate and generates secondary electrons via protein−surface collisions (cpp = counts per pixel).

energies since the instrument was designed to operate at a higher ion energy of ∼35 V.

Effect of DC Offset Voltage across First Hexapole. The "RF DC offset 1" parameter that defines the DC offset voltage across the first hexapole displays a similar behavior as "ion energy". As this voltage increases, the potential difference between the first hexapole and its exit lens (aperture 1) is increased and leading to an increase in the axial ion energy of ions entering the pusher. Expectedly, this leads to a shift in the spatial distribution of the ion cloud toward the right side of the detector (Figure 4c).

Figure 4c is generated from the data recorded at a fixed "ion energy" settings of 10 V, which resulted in spatial intensity distribution to be very sensitive to small variation in the DC offset voltage of the first hexapole. Figure S4 (Supporting Information) is generated for the exactly same "RF DC offset 1" values used in Figure 4c but for a higher "ion energy" of 40 V, and it is observed that the intensity profile of ions is less sensitive to the DC offset of the first hexapole.

Effect of Reflectron Voltage. The "Reflectron" sets the voltage at the rear of the reflectron. A change in the reflectron voltage does not affect θ, but this voltage does define the point from which the ion beam gets reflected back to the detector. For higher reflectron voltages, this turn-around position is closer to the detector and results in the ion beam hitting more toward the left side of the detector (Figure 4d).

General Observations. Equation of θ can be rewritten as

$$\vartheta = \tan^{-1}\frac{v_z}{v_x} = \tan^{-1}\sqrt{\frac{V_z}{V_x}} \qquad (2)$$

where V_x and V_z are the acceleration potential components in x- and z-directions, respectively.[13] Equation 2 clearly shows that θ is independent of the mass of the protein; hence, the same spatial distribution is expected to be observed for different proteins under identical ion optics conditions. Figure S5 (Supporting Information) shows the spatial distribution of the ion cloud corresponding to different proteins of masses from 12.4 to 223.8 kDa acquired under similar voltage conditions, and the spatial profiles look similar as expected.
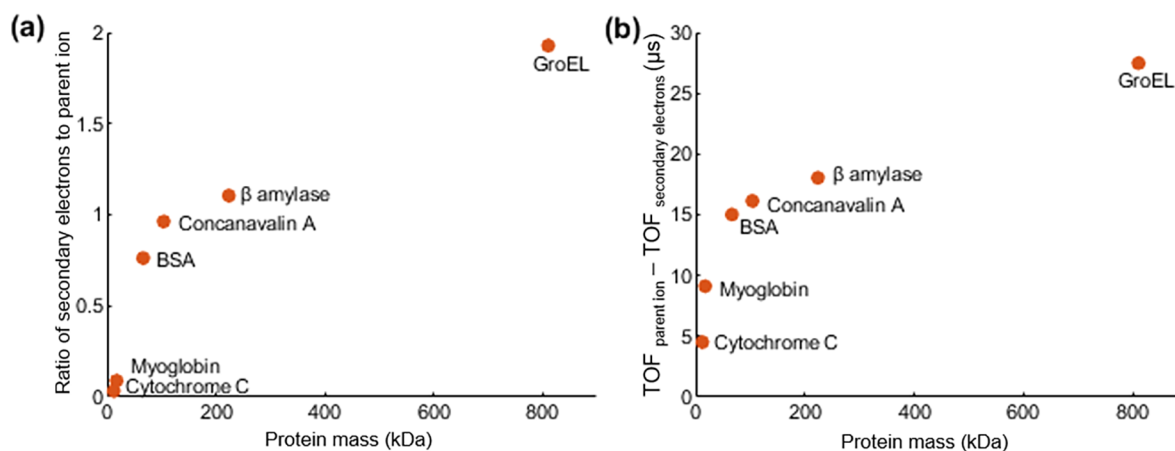
Figure 6. (a) Ratio of the number of surface emitted secondary electrons to the parent ion plotted for proteins of different masses. The number of parent ions and secondary electrons reaching the detector is calculated by dividing the signal intensity of each by the average number of pixels activated. (b) Difference in the mean arrival time of secondary electrons and parent ion plotted as a function of mass of the protein.

Figure S6 (Supporting Information) is generated using the exact same ion optical conditions used in Figure 4 but with a different protein—conalbumin (77 kDa), and the spatial distributions are observed to be identical to those of cytochrome *c* except for axial ion energy. This is due to the origin of mass-independent secondary particles at higher axial energies, which will be discussed in the next section.

All of the experimental data show good agreement with the SIMION ion optical simulation results. Simulated ion trajectories of cytochrome *c* for different TOF tube voltages are shown in Supporting Information (Figure S7).

Visualization of Secondary Electrons Generated by Protein−Surface Interaction. In this section, the imaging capability of the TPX is further exploited to determine the origin of the unexpected TOF signal observed with flight times less than the corresponding parent protein. Figure 5a shows the TOF spectrum of GroEL recorded at different "ion energy" voltage settings from 10 to 50 V, while the corresponding TPX images for all the arriving ions are shown in Figure 5b. In addition to the intact GroEL signal (red trace), an additional spectral distribution is observed at lower TOF values that increases in abundance with increasing axial ion energy (blue trace). For an ion energy of 50 V, two distinct distributions are observed in both the mass spectrum and total ion image. Figure 5c shows the corresponding TPX images for the red and blue flight times indicated in Figure 5a and demonstrates the spatial separation of these two populations at the detector. As expected, high TOF intact GroEL signal shows a shift in impact position to the right of the detector with an increase in axial ion energy. In contrast, the low TOF secondary particle distribution does not exhibit a shift in impact position with increasing axial ion energy. Similar spectra and TPX images were also observed at high axial ion energies for a series of different protein ions (Supporting Information Figure S8). The formation of this low TOF signal at high axial energy was reproduced on a second, unmodified LCT equipped with the standard detector (Supporting Information Figure S9). Surprisingly, the impact position of this secondary population was also observed to be insensitive to all other instrument parameters including the reflectron and TOF tube voltages (Supporting Information Figure S10).

Insensitivity to both axial ion energy and the reflector voltage allows exclusion of two possible sources of this secondary population. First, the possibility of secondary particle formation prior to the pusher can be excluded as the axial ion energy does not alter the impact position of this secondary population. The possibility of secondary particle formation inside the reflectron can also be excluded due to the fact that neither the flight time of the ions nor their impact position changes with the reflectron voltages. Such behavior would be otherwise expected upon the creation of ions having different *m/z* values within the decelerating/accelerating field of the reflectron.

Another possibility considered is the occurrence of metastable fragmentation between the reflectron exit and the TPX. However, this is excluded for the following reasons: (i) after metastable fragmentation in the field-free region, fragments travel at the same velocity as the precursor ion and would have identical arrival times and impact positions at the detector (ignoring the small radial kinetic energy discrepancy resulting from dissociation);[19,58] (ii) the spatial profile of metastable ions are expected to also be sensitive to voltages prior to the TOF measurement in a similar manner as their parent ions. Nonetheless, the above observations provide strong circumstantial evidence for the generation of the secondary particles in the post-reflectron region.

SIMION simulations were employed to investigate these effects further. It was observed that the mean TOF of the secondary particles was very close to the simulated TOF of the intact protein ions to reach the exit of the reflectron. Figure 5d plots the experimentally measured mean TOF of the secondary particle distribution (blue trace) and the time difference between the simulated TOF of the protein ions to the exit of the reflectron and the experimentally measured TOF of the secondary particles (orange trace). Interestingly, there is very little dependency of the time difference plotted as the orange trace in Figure 5d on the mass (and thus *m/z*) of the protein, suggesting the identity of the secondary population is the same regardless of the protein being analyzed. This led us to believe the source of this low TOF signal was the creation of secondary electrons by protein−surface collisions near the reflectron exit. As a result of surface interaction of the primary beam, positively charged/neutral protein fragments and surface emitted positively charge ions/negatively charged ions/neutrals could also be generated. However, all of these possibilities were excluded due to the lower TOF of the

secondary particles compared to the parent ions in the field free region. The LCT contains an uncoated stainless steel support plate placed between the first reflectron grid and detector. The position of this support plate is such that it lines up with the detector (Figure 5e). At higher axial higher ion energies, the flight angle becomes wider (lower θ) and leads to an increased probability of the ion cloud to hit the support plate and to generate more secondary electrons from protein−surface collisions. Further evidence for the support plate as the source of this additional signal is the close match in the overlapping area of the support plate with the detector (9.5 mm) and the size of the secondary particle image on the TPX (∼9.4 mm). The comparison between the results from the experiments and LCT ion optics model suggests that an energy of ∼4 meV is enough to accelerate the secondary electrons from the support plate to the detector with a mean flight time of ∼9.5 μs.

The extent of the surface emitted secondary electrons and its dependency on the parent protein ions were studied for different proteins under similar ion optical conditions; ion energy = 50 V, reflectron = 1000 V, TOF tube = 4600 V, RF DC offset 1 = 10 V. As expected, it was observed that the spatial profile of all proteins looks similar for same voltage settings (Supporting Information Figure S8). However, the ratio of secondary electrons to parent ion intensity shows an increasing trend with the mass of the protein (Figure 6a). Two possible contributors to this are the reduced detection efficiency (ion-to-electron conversion) of higher m/z ions, an effect known to arise when using MCP-based detectors, and the possibility of higher secondary electron yields per surface impact with increasing m/z of the parent protein ion.[59,60]

Figure 6b shows the relationship between the mass of the protein and the difference between time-of-arrival of parent ion and secondary electrons. The time-of-arrival measured at the detector corresponding to the secondary electrons is the sum of time taken by the primary beam to travel from pusher to support plate and the surface emitted electrons to reach the detector. Hence, an increasing trend in TOF difference between parent and secondary electron with the size of the protein is expected, which matches with the experimental results.

CONCLUSION

In this work, we have described the first implementation of a TPX active pixel detector coupled to an ESI-equipped mass spectrometer modified for high mass transmission. This new experimental setup allows the detection and ion imaging of multiply charged protein complexes of molecular weight in excess of 800 kDa generated by native MS. By utilizing the single-ion imaging capabilities of the TPX detector, the spatial distribution of ions at the detector surface has been studied as a function of various ion optical parameters. The combination of both space- and time-resolved detection was critical to understand the origin of a mysterious signal observed with high entrance energies into the pusher as secondary electrons produced by protein−surface collisions at the exit of the reflectron. The unique imaging capability of TPX allows for more detailed insight into the functionality of each ion optical element within the mass spectrometer. This makes TPX a suitable tool for the optimization of newly developed mass spectrometers and allows for more direct comparisons between the ion optics simulations and experimental data.

This work supports previous studies highlighting the utility of the TPX detector, and other similar detectors such as pixel imaging mass spectrometry (PImMS) camera for simultaneously imaging of ions with different arrival times and for studying ion optical processes.[32,61] Active pixel detectors are demonstrated to offer significant advantages over traditional charge-coupled-device-based approaches that are widely used in ion imaging applications such as velocity map imaging.[46,62]

The TPX detector used for this work is limited by a moderate time resolution (20 ns here, at best 10 ns) and single-stop detection for each pixel that can bias the detection of ions with a low TOF at high count rates. Future studies will benefit from the implementation of the next generation Timepix3 detector that among other advantages offers 1.56 ns time resolution, per-pixel multi-hit functionality and kHz readout rates.[63−66]

■ ASSOCIATED CONTENT

ⓈI Supporting Information

The Supporting Information is available free of charge at https://pubs.acs.org/doi/10.1021/jasms.0c00412.

Figures S1−S10 (PDF)

■ AUTHOR INFORMATION

Corresponding Authors

Shane R. Ellis − *Maastricht MultiModal Molecular Imaging (M4I) Institute, Division of Imaging Mass Spectrometry (IMS), Maastricht University, 6229 ER Maastricht, The Netherlands; Molecular Horizons and School of Chemistry and Molecular Bioscience, University of Wollongong, Wollongong, NSW 2522, Australia;* ⓘ orcid.org/0000-0002-3326-5991; Email: sellis@uow.edu.au

Ron M. A. Heeren − *Maastricht MultiModal Molecular Imaging (M4I) Institute, Division of Imaging Mass Spectrometry (IMS), Maastricht University, 6229 ER Maastricht, The Netherlands;* ⓘ orcid.org/0000-0002-6533-7179; Email: r.heeren@maastrichtuniversity.nl

Authors

Anjusha Mathew − *Maastricht MultiModal Molecular Imaging (M4I) Institute, Division of Imaging Mass Spectrometry (IMS), Maastricht University, 6229 ER Maastricht, The Netherlands*

Ronald Buijs − *NWO Institute AMOLF, 1098 XG Amsterdam, The Netherlands*

Gert B. Eijkel − *Maastricht MultiModal Molecular Imaging (M4I) Institute, Division of Imaging Mass Spectrometry (IMS), Maastricht University, 6229 ER Maastricht, The Netherlands*

Frans Giskes − *Maastricht MultiModal Molecular Imaging (M4I) Institute, Division of Imaging Mass Spectrometry (IMS), Maastricht University, 6229 ER Maastricht, The Netherlands*

Andrey Dyachenko − *Biomolecular Mass Spectrometry and Proteomics, Bijvoet Centre for Biomolecular Research and Utrecht Institute for Pharmaceutical Sciences, Utrecht University, 3584 CH Utrecht, The Netherlands; Netherlands Proteomics Center, 3584 CH Utrecht, The Netherlands*

Jerre van der Horst − *MS Vision, 1322 AM Almere, The Netherlands*

Dimitry Byelov − *Amsterdam Scientific Instruments (ASI), 1098 XG Amsterdam, The Netherlands*

Dirk-Jan Spaanderman − *NWO Institute AMOLF, 1098 XG Amsterdam, The Netherlands*

Albert J. R. Heck − *Biomolecular Mass Spectrometry and Proteomics, Bijvoet Centre for Biomolecular Research and Utrecht Institute for Pharmaceutical Sciences, Utrecht University, 3584 CH Utrecht, The Netherlands; Netherlands Proteomics Center, 3584 CH Utrecht, The Netherlands;* ⦿ orcid.org/0000-0002-2405-4404

Tiffany Porta Siegel − *Maastricht MultiModal Molecular Imaging (M4I) Institute, Division of Imaging Mass Spectrometry (IMS), Maastricht University, 6229 ER Maastricht, The Netherlands;* ⦿ orcid.org/0000-0001-5454-1863

Complete contact information is available at:
https://pubs.acs.org/10.1021/jasms.0c00412

Notes

The authors declare no competing financial interest.

■ REFERENCES

(1) Heck, A. J. Native mass spectrometry: a bridge between interactomics and structural biology. *Nat. Methods* **2008**, *5* (11), 927−33.

(2) Heck, A. J.; Van Den Heuvel, R. H. Investigation of intact protein complexes by mass spectrometry. *Mass Spectrom. Rev.* **2004**, *23* (5), 368−89.

(3) Sharon, M.; Robinson, C. V. The role of mass spectrometry in structure elucidation of dynamic protein complexes. *Annu. Rev. Biochem.* **2007**, *76*, 167−93.

(4) Yin, S.; Loo, J. A. Top-down mass spectrometry of supercharged native protein−ligand complexes. *Int. J. Mass Spectrom.* **2011**, *300* (2−3), 118−122.

(5) Gault, J.; Liko, I.; Landreh, M.; Shutin, D.; Bolla, J. R.; Jefferies, D.; Agasid, M.; Yen, H.-Y.; Ladds, M. J. G. W.; Lane, D. P.; Khalid, S.; Mullen, C.; Remes, P. M.; Huguet, R.; McAlister, G.; Goodwin, M.; Viner, R.; Syka, J. E.P.; Robinson, C. V. Combining native and 'omics' mass spectrometry to identify endogenous ligands bound to membrane proteins. *Nat. Methods* **2020**, *17* (5), 505−508.

(6) Hanson, C. L.; Robinson, C. V. Protein-nucleic acid interactions and the expanding role of mass spectrometry. *J. Biol. Chem.* **2004**, *279* (24), 24907−10.

(7) van de Waterbeemd, M.; Fort, K. L.; Boll, D.; Reinhardt-Szyba, M.; Routh, A.; Makarov, A.; Heck, A. J. High-fidelity mass analysis unveils heterogeneity in intact ribosomal particles. *Nat. Methods* **2017**, *14* (3), 283−286.

(8) Tito, M. A.; Tars, K.; Valegard, K.; Hajdu, J.; Robinson, C. V. Electrospray time-of-flight mass spectrometry of the intact MS2 virus capsid. *J. Am. Chem. Soc.* **2000**, *122* (14), 3550−3551.

(9) Snijder, J.; Rose, R. J.; Veesler, D.; Johnson, J. E.; Heck, A. J. Studying 18 MDa virus assemblies with native mass spectrometry. *Angew. Chem., Int. Ed.* **2013**, *52* (14), 4020−3.

(10) Wilm, M.; Mann, M. Analytical properties of the nano-electrospray ion source. *Anal. Chem.* **1996**, *68* (1), 1−8.

(11) Nesatyy, V. J. Mass spectrometry evaluation of the solution and gas-phase binding properties of noncovalent protein complexes. *Int. J. Mass Spectrom.* **2002**, *221* (2), 147−161.

(12) Verentchikov, A. N.; Ens, W.; Standing, K. G. Reflecting time-of-flight mass spectrometer with an electrospray ion source and orthogonal extraction. *Anal. Chem.* **1994**, *66* (1), 126−33.

(13) Guilhaus, M.; Selby, D.; Mlynski, V. Orthogonal acceleration time-of-flight mass spectrometry. *Mass Spectrom. Rev.* **2000**, *19* (2), 65−107.

(14) Tahallah, N.; Pinkse, M.; Maier, C. S.; Heck, A. J. The effect of the source pressure on the abundance of ions of noncovalent protein assemblies in an electrospray ionization orthogonal time-of-flight instrument. *Rapid Commun. Mass Spectrom.* **2001**, *15* (8), 596−601.

(15) Sobott, F.; Hernandez, H.; McCammon, M. G.; Tito, M. A.; Robinson, C. V. A tandem mass spectrometer for improved transmission and analysis of large macromolecular assemblies. *Anal. Chem.* **2002**, *74* (6), 1402−7.

(16) van den Heuvel, R. H.; van Duijn, E.; Mazon, H.; Synowsky, S. A.; Lorenzen, K.; Versluis, C.; Brouns, S. J.; Langridge, D.; van der Oost, J.; Hoyes, J.; Heck, A. J. Improving the performance of a quadrupole time-of-flight instrument for macromolecular mass spectrometry. *Anal. Chem.* **2006**, *78* (21), 7473−83.

(17) Rose, R. J.; Damoc, E.; Denisov, E.; Makarov, A.; Heck, A. J. High-sensitivity Orbitrap mass analysis of intact macromolecular assemblies. *Nat. Methods* **2012**, *9* (11), 1084−6.

(18) Ladislas Wiza, J. Microchannel plate detectors. *Nucl. Instrum. Methods* **1979**, *162* (1−3), 587−601.

(19) Guilhaus, M. Special feature: Tutorial. Principles and instrumentation in time-of-flight mass spectrometry. Physical and instrumental concepts. *J. Mass Spectrom.* **1995**, *30* (11), 1519−1532.

(20) Wang, C.-C.; Lai, Y.-H.; Ou, Y.-M.; Chang, H.-T.; Wang, Y.-S. Critical factors determining the quantification capability of matrix-assisted laser desorption/ionization−time-of-flight mass spectrometry. *Philos. Trans. R. Soc., A* **2016**, *374* (2079), 20150371.

(21) Llopart, X.; Ballabriga, R.; Campbell, M.; Tlustos, L.; Wong, W. Timepix, a 65k programmable pixel readout chip for arrival time, energy and/or photon counting measurements. *Nucl. Instrum. Methods Phys. Res., Sect. A* **2007**, *581* (1−2), 485−494.

(22) Campbell, M.; Collaboration, M.. 10 years of the Medipix2 Collaboration. *Nucl. Instrum. Methods Phys. Res., Sect. A* **2011**, *633*, S1−S10.

(23) Esposito, M.; Jakubek, J.; Mettivier, G.; Pospisil, S.; Russo, P.; Solc, J. Energy sensitive Timepix silicon detector for electron imaging. *Nucl. Instrum. Methods Phys. Res., Sect. A* **2011**, *652* (1), 458−461.

(24) Wong, W.; Alozy, J.; Ballabriga, R.; Campbell, M.; Kremastiotis, I.; Llopart, X.; Poikela, T.; Sriskaran, V.; Tlustos, L.; Turecek, D. Introducing Timepix2, a frame-based pixel detector readout ASIC measuring energy deposition and arrival time. *Radiat. Meas.* **2020**, *131*, 106230.

(25) Al Darwish, R.; Marcu, L.; Bezak, E. Overview of current applications of the Timepix detector in spectroscopy, radiation and medical physics. *Appl. Spectrosc. Rev.* **2020**, *55* (3), 243−261.

(26) Bamberger, C.; Renz, U.; Bamberger, A. Digital imaging mass spectrometry. *J. Am. Soc. Mass Spectrom.* **2011**, *22* (6), 1079−87.

(27) Jungmann, J. H.; MacAleese, L.; Visser, J.; Vrakking, M. J.; Heeren, R. M. High dynamic range bio-molecular ion microscopy with the Timepix detector. *Anal. Chem.* **2011**, *83* (20), 7888−94.

(28) Clark, A. T.; Crooks, J. P.; Sedgwick, I.; Turchetta, R.; Lee, J. W.; John, J. J.; Wilman, E. S.; Hill, L.; Halford, E.; Slater, C. S.; Winter, B.; Yuen, W. H.; Gardiner, S. H.; Lipciuc, M. L.; Brouard, M.; Nomerotski, A.; Vallance, C. Multimass velocity-map imaging with the Pixel Imaging Mass Spectrometry (PImMS) sensor: an ultra-fast event-triggered camera for particle imaging. *J. Phys. Chem. A* **2012**, *116* (45), 10897−903.

(29) Ellis, S. R.; Jungmann, J. H.; Smith, D. F.; Soltwisch, J.; Heeren, R. M. Enhanced Detection of High-Mass Proteins by Using an Active Pixel Detector. *Angew. Chem., Int. Ed.* **2013**, *52* (43), 11261−11264.

(30) Jungmann, J. H.; Smith, D. F.; Kiss, A.; MacAleese, L.; Buijs, R.; Heeren, R. M. A. An in-vacuum, pixelated detection system for mass spectrometric analysis and imaging of macromolecules. *Int. J. Mass Spectrom.* **2013**, *341*, 34−44.

(31) Kiss, A.; Smith, D. F.; Jungmann, J. H.; Heeren, R. M. Cluster secondary ion mass spectrometry microscope mode mass spectrometry imaging. *Rapid Commun. Mass Spectrom.* **2013**, *27* (24), 2745−2750.

(32) Ellis, S. R.; Soltwisch, J.; Heeren, R. M. Time-resolved imaging of the MALDI linear-TOF ion cloud: direct visualization and exploitation of ion optical phenomena using a position- and time-sensitive detector. *J. Am. Soc. Mass Spectrom.* **2014**, *25* (5), 809−19.

(33) Soltwisch, J.; Goritz, G.; Jungmann, J. H.; Kiss, A.; Smith, D. F.; Ellis, S. R.; Heeren, R. M. MALDI mass spectrometry imaging in microscope mode with infrared lasers: bypassing the diffraction limits. *Anal. Chem.* **2014**, *86* (1), 321−5.

(34) Syed, S. U.; Eijkel, G. B.; Kistemaker, P.; Ellis, S.; Maher, S.; Smith, D. F.; Heeren, R. M. Experimental investigation of the 2D ion beam profile generated by an ESI octopole-QMS system. *J. Am. Soc. Mass Spectrom.* **2014**, *25* (10), 1780−7.

(35) Jencic, B.; Sepec, L.; Vavpetic, P.; Kelemen, M.; Rupnik, Z.; Vencelj, M.; Vogel-Mikus, K.; Ogrinc Potocnik, N.; Ellis, S. R.; Heeren, R. M.A.; Pelicon, P. Stigmatic imaging of secondary ions in MeV-SIMS spectrometry by linear Time-of-Flight mass spectrometer and the TimePix detector. *Nucl. Instrum. Methods Phys. Res., Sect. B* **2019**, *452*, 1−6.

(36) Sobott, F.; Robinson, C. V. Characterising electrosprayed biomolecules using tandem-MS—the noncovalent GroEL chaperonin assembly. *Int. J. Mass Spectrom.* **2004**, *236* (1−3), 25−32.

(37) van Duijn, E.; Simmons, D. A.; van den Heuvel, R. H.; Bakkes, P. J.; van Heerikhuizen, H.; Heeren, R. M.; Robinson, C. V.; van der Vies, S. M.; Heck, A. J. Tandem mass spectrometry of intact GroEL-substrate complexes reveals substrate-specific conformational changes in the trans ring. *J. Am. Chem. Soc.* **2006**, *128* (14), 4694−702.

(38) Uetrecht, C.; Watts, N. R.; Stahl, S. J.; Wingfield, P. T.; Steven, A. C.; Heck, A. J. Subunit exchange rates in Hepatitis B virus capsids are geometry- and temperature-dependent. *Phys. Chem. Chem. Phys.* **2010**, *12* (41), 13368−71.

(39) Brasch, M.; de la Escosura, A.; Ma, Y.; Uetrecht, C.; Heck, A. J.; Torres, T.; Cornelissen, J. J. Encapsulation of phthalocyanine supramolecular stacks into virus-like particles. *J. Am. Chem. Soc.* **2011**, *133* (18), 6878−6881.

(40) Uetrecht, C.; Barbu, I. M.; Shoemaker, G. K.; Van Duijn, E.; Heck, A. J. Interrogating viral capsid assembly with ion mobility−mass spectrometry. *Nat. Chem.* **2011**, *3* (2), 126.

(41) Snijder, J.; Uetrecht, C.; Rose, R. J.; Sanchez-Eugenia, R.; Marti, G. A.; Agirre, J.; Guerin, D. M. A.; Wuite, G. J. L.; Heck, A. J. R.; Roos, W. H. Probing the biophysical interplay between a viral genome and its capsid. *Nat. Chem.* **2013**, *5* (6), 502−509.

(42) Vykydal, Z.; Visschers, J.; Tezcan, D. S.; De Munck, K.; Borgers, T.; Ruythooren, W.; De Moor, P. The RELAXd project: Development of four-side tilable photon-counting imagers. *Nucl. Instrum. Methods Phys. Res., Sect. A* **2008**, *591* (1), 241−244.

(43) Schmidt, A.; Bahr, U.; Karas, M. Influence of pressure in the first pumping stage on analyte desolvation and fragmentation in nano-ESI MS. *Anal. Chem.* **2001**, *73* (24), 6040−6.

(44) Chernushevich, I. V.; Thomson, B. A. Collisional cooling of large ions in electrospray mass spectrometry. *Anal. Chem.* **2004**, *76* (6), 1754−60.

(45) van Duijn, E.; Bakkes, P. J.; Heeren, R. M.; van den Heuvel, R. H.; van Heerikhuizen, H.; van der Vies, S. M.; Heck, A. J. Monitoring macromolecular complexes involved in the chaperonin-assisted protein folding cycle by mass spectrometry. *Nat. Methods* **2005**, *2* (5), 371−6.

(46) Jungmann, J. H.; Gijsbertsen, A.; Visser, J.; Visschers, J.; Heeren, R. M.; Vrakking, M. J. A new imaging method for

understanding chemical dynamics: efficient slice imaging using an in-vacuum pixel detector. *Rev. Sci. Instrum.* **2010**, *81* (10), 103112.

(47) Akiba, K.; Artuso, M.; Badman, R.; Borgia, A.; Bates, R.; Bayer, F.; van Beuzekom, M.; Buytaert, J.; Cabruja, E.; Campbell, M.; Collins, P.; Crossley, M.; Dumps, R.; Eklund, L.; Esperante, D.; Fleta, C.; Gallas, A.; Gandelman, M.; Garofoli, J.; Gersabeck, M.; Gligorov, V. V.; Gordon, H.; Heijne, E. H.M.; Heijne, V.; Hynds, D.; John, M.; Leflat, A.; Ferre Llin, L.; Llopart, X.; Lozano, M.; Maneuski, D.; Michel, T.; Nicol, M.; Needham, M.; Parkes, C.; Pellegrini, G.; Plackett, R.; Poikela, T.; Rodrigues, E.; Stewart, G.; Wang, J.; Xing, Z. Charged particle tracking with the Timepix ASIC. *Nucl. Instrum. Methods Phys. Res., Sect. A* **2012**, *661* (1), 31−49.

(48) Anton, G.; Gebert, U.; Michel, T.; Rugheimer, T. K. A hybrid photodetector using the Timepix semiconductor assembly for photoelectron detection. *Nucl. Instrum. Methods Phys. Res., Sect. A* **2009**, *602* (1), 205−208.

(49) Furch, F. J.; Dura, J.; Tremsin, A. S.; Vallerga, J.; Schulz, C. P.; Rouzee, A.; Vrakking, M. J. J. Ion-ion coincidence imaging at high event rate using an in-vacuum pixel detector. *J. Chem. Phys.* **2017**, *147* (1), 013919.

(50) Rostom, A. A.; Fucini, P.; Benjamin, D. R.; Juenemann, R.; Nierhaus, K. H.; Hartl, F. U.; Dobson, C. M.; Robinson, C. V. Detection and selective dissociation of intact ribosomes in a mass spectrometer. *Proc. Natl. Acad. Sci. U. S. A.* **2000**, *97* (10), 5185−90.

(51) Smith, R. D.; Cheng, X.; Brace, J. E.; Hofstadler, S. A.; Anderson, G. A. Trapping, Detection and Reaction of Very Large Single Molecular-Ions by Mass-Spectrometry. *Nature* **1994**, *369* (6476), 137−139.

(52) Bruce, J. E.; Anderson, G. A.; Udseth, H. R.; Smith, R. D. Large Molecule Characterization Based upon Individual Ion Detection with Electrospray Ionization-FTICR Mass Spectrometry. *Anal. Chem.* **1998**, *70* (3), 519−25.

(53) Makarov, A.; Denisov, E. Dynamics of ions of intact proteins in the Orbitrap mass analyzer. *J. Am. Soc. Mass Spectrom.* **2009**, *20* (8), 1486−95.

(54) Kafader, J. O.; Melani, R. D.; Senko, M. W.; Makarov, A. A.; Kelleher, N. L.; Compton, P. D. Measurement of Individual Ions Sharply Increases the Resolution of Orbitrap Mass Spectra of Proteins. *Anal. Chem.* **2019**, *91* (4), 2776−2783.

(55) Kafader, J. O.; Melani, R. D.; Durbin, K. R.; Ikwuagwu, B.; Early, B. P.; Fellers, R. T.; Beu, S. C.; Zabrouskov, V.; Makarov, A. A.; Maze, J. T.; Shinholt, D. L.; Yip, P. F.; Tullman-Ercek, D.; Senko, M. W.; Compton, P. D.; Kelleher, N. L. Multiplexed mass spectrometry of individual ions improves measurement of proteoforms and their complexes. *Nat. Methods* **2020**, *17* (4), 391−394.

(56) Worner, T. P.; Snijder, J.; Bennett, A.; Agbandje-McKenna, M.; Makarov, A. A.; Heck, A. J. R. Resolving heterogeneous macromolecular assemblies by Orbitrap-based single-particle charge detection mass spectrometry. *Nat. Methods* **2020**, *17* (4), 395−398.

(57) Beuhler, R.; Friedman, L. Low noise, high voltage secondary emission ion detector for polyatomic ions. *Int. J. Mass Spectrom. Ion Phys.* **1977**, *23* (2), 81−97.

(58) Versluis, C.; van der Staaij, A.; Stokvis, E.; Heck, A. J.; de Craene, B. Metastable ion formation and disparate charge separation in the gas-phase dissection of protein assemblies studied by orthogonal time-of-flight mass spectrometry. *J. Am. Soc. Mass Spectrom.* **2001**, *12* (3), 329−336.

(59) Brunelle, A.; Chaurand, P.; Della-Negra, S.; Le Beyec, Y.; Parilis, E. Secondary Electron Emission Yields from a CsI Surface Under Impacts of Large Molecules at Low Velocities (5× 103− 7× 104 ms− 1). *Rapid Commun. Mass Spectrom.* **1997**, *11* (4), 353−362.

(60) Liu, R.; Li, Q.; Smith, L. M. Detection of large ions in time-of-flight mass spectrometry: effects of ion mass and acceleration voltage on microchannel plate detector response. *J. Am. Soc. Mass Spectrom.* **2014**, *25* (8), 1374−83.

(61) Brouard, M.; Halford, E.; Lauer, A.; Slater, C. S.; Winter, B.; Yuen, W. H.; John, J. J.; Hill, L.; Nomerotski, A.; Clark, A.; Crooks, J.; Sedgwick, I.; Turchetta, R.; Lee, J. W.; Vallance, C.; Wilman, E. The application of the fast, multi-hit, pixel imaging mass spectrometry

sensor to spatial imaging mass spectrometry. *Rev. Sci. Instrum.* **2012**, *83* (11), 114101.

(62) Vallance, C. Multi-mass velocity-map imaging studies of photoinduced and electron-induced chemistry. *Chem. Commun. (Cambridge, U. K.)* **2019**, *55* (45), 6336−6352.

(63) Poikela, T.; Plosila, J.; Westerlund, T.; Campbell, M.; De Gaspari, M.; Llopart, X.; Gromov, V.; Kluit, R.; van Beuzekom, M.; Zappon, F.; Zivkovic, V.; Brezina, C.; Desch, K.; Fu, Y.; Kruth, A. Timepix3: a 65K channel hybrid pixel readout chip with simultaneous ToA/ToT and sparse readout. *J. Instrum.* **2014**, *9* (05), C05013.

(64) Frojdh, E.; Campbell, M.; De Gaspari, M.; Kulis, S.; Llopart, X.; Poikela, T.; Tlustos, L. Timepix3: first measurements and characterization of a hybrid-pixel detector working in event driven mode. *J. Instrum.* **2015**, *10* (01), C01039.

(65) Zhao, A.; van Beuzekom, M.; Bouwens, B.; Byelov, D.; Chakaberia, I.; Cheng, C.; Maddox, E.; Nomerotski, A.; Svihra, P.; Visser, J.; Vrba, V.; Weinacht, T. Coincidence velocity map imaging using Tpx3Cam, a time stamping optical camera with 1.5 ns timing resolution. *Rev. Sci. Instrum.* **2017**, *88* (11), 113104.

(66) Bergmann, B.; Billoud, T.; Burian, P.; Broulim, P.; Leroy, C.; Lesmes, C.; Manek, P.; Meduna, L.; Pospisil, S.; Sopczak, A.; Suk, M. Relative luminosity measurement with Timepix3 in ATLAS. *J. Instrum.* **2020**, *15* (1), C01039.